Journal of Materials Chemistry A

PAPER

View Article Online
View Journal | View Issue





Cite this: J. Mater. Chem. A, 2018, 6, 14324

# 2D holey cobalt sulfide nanosheets derived from metal–organic frameworks for high-rate sodium ion batteries with superior cyclability†

Yanfeng Dong,[a] Wen Shi,[b] Pengfei Lu,[a] Jieqiong Qin,[ac] Shuanghao Zheng,[acd] Bingsen Zhang,[b] Xinhe Bao[ad] and Zhong-Shuai Wu*[a]

Received 13th June 2018
Accepted 2nd July 2018

DOI: 10.1039/c8ta05612a

rsc.li/materials-a

Sodium ion batteries (SIBs) for large-scale grid applications are facing great challenges in terms of development of high-performance electrode materials and screening of suitable electrolytes. Herein, a versatile and scalable protocol for synthesizing two-dimensional (2D) holey cobalt sulfide (h-$Co_4S_3$) nanosheets is demonstrated for high-rate and long-life SIBs in an ether-based electrolyte of 1.0 M $NaCF_3SO_3$ in diglyme. The 2D h-$Co_4S_3$ nanosheets are prepared by sulfuration of leaf-like cobalt based metal–organic frameworks (CoMOFs), and subsequent annealing treatment. Benefiting from the nanosheet nature of in-plane nanopores (10–30 nm), ultra-thinness (<30 nm), crumpled morphology, and micron-scale lateral size that can provide more active sites and enhanced sodiation/desodiation kinetics, the resulting h-$Co_4S_3$ nanosheets achieve a high reversible capacity of 571 mA h $g^{-1}$ at 0.1 A $g^{-1}$, and long-life cycling stability with a retention of 80% after 400 cycles for SIBs. Furthermore, theoretical simulation reveals the enhanced structural stability of h-$Co_4S_3$ nanosheets with a lower binding energy (0.31 eV) of the Co–O bond in the ether-based electrolyte than that in the carbonate-based electrolyte. Notably, the h-$Co_4S_3$ anode offers an exceptional rate capacity of 257 mA h $g^{-1}$ at 12 A $g^{-1}$, outperforming most reported cobalt sulfide-based anodes. This strategy will pave a new way to rationally construct MOF-derived 2D nanostructures for various energy-related applications.

## Introduction

Sodium ion batteries (SIBs) are one of the most promising alternatives to lithium ion batteries (LIBs) for various electronic and large-scale grid storage applications due to the natural abundance, low cost, high theoretical capacity and low redox potentials ($E_{Na^+/Na} = -2.7$ V) of sodium.[1–3] Unfortunately, the larger ionic radius of $Na^+$ (1.02 Å) in comparison with $Li^+$ (0.76 Å) results in huge volume expansion, sluggish reaction kinetics and unsatisfactory electroactivity.[4,5] Therefore, exploiting the working of advanced electrodes in suitable electrolytes is highly required for the coming era of SIBs.

So far, great efforts have been made to develop nanostructured cathode materials, *e.g.*, $Na_3V_2(PO_4)_3$,[6] $Na_3V_2O_2(PO_4)_2F$,[7] Prussian blue,[8] β-$NaMnO_2$,[9] and advanced anodes of antimony,[10] metallic sulfides,[11–13] and metallic oxides,[14,15] for SIBs. Among them, cobalt sulfides (*e.g.*, $CoS_2$, $Co_8S_9$, and $Co_4S_3$) have attracted ever-increasing attention because they exhibit higher first-cycle efficiency, a higher theoretical capacity of 500–700 mA h $g^{-1}$ than carbon anodes (200–450 mA h $g^{-1}$),[1,16,17] and weaker interaction of Co–S bonds in cobalt sulfides than Co–O bonds in cobalt oxides for SIBs.[2,17–19] However, cobalt sulfides suffer from poor conductivity and large volume expansion during sodiation/desodiation, resulting in low capacity and fast capacity fade.

One effective way to overcome this issue is to rationally design well-defined cobalt sulfide micro/nanostructures with large accessible surface areas and void spaces to enhance kinetics and accommodate their volume change for structural integrity,[20,21] *e.g.*, $Co_3S_4$@polyaniline nanotubes,[22] CoS nanoplates on reduced graphene oxide (rGO),[19] hollow $CoS_2$ octahedrons and $CoS_x$ nanospheres.[23,24] Recently, two-dimensional (2D) nanosheets with a large aspect ratio, highly exposed surface and extremely reduced diffusion distances have been shown to hold promise for energy storage.[20,25–29] Unfortunately, restacking of 2D nanosheets during synthesis and electrode manufacturing irreversibly decreases the effective surface area and blocks electrolyte diffusion into the interior of electrodes. In this regard, the introduction of nanopores into the plane of 2D nanosheets would significantly accommodate volume

[a]Dalian National Laboratory for Clean Energy, Dalian Institute of Chemical Physics, Chinese Academy of Sciences, 457 Zhongshan Road, Dalian 116023, China. E-mail: wuzs@dicp.ac.cn

[b]Shenyang National Laboratory for Materials Science, Institute of Metal Research, Chinese Academy of Sciences, 72 Wenhua Road, Shenyang 110016, China

[c]University of Chinese Academy of Sciences, 19 A Yuquan Rd, Shijingshan District, Beijing, 100049, China

[d]State Key Laboratory of Catalysis, Dalian Institute of Chemical Physics, Chinese Academy of Sciences, 457 Zhongshan Road, Dalian 116023, China

† Electronic supplementary information (ESI) available. See DOI: 10.1039/c8ta05612a

expansions and stabilize electrodes for improving long-cycling life, facilitate ion diffusion kinetics for high powder density, and even accelerate ion diffusion in thick electrodes for high energy density.[30,31] For example, holey $Co_3O_4$ nanosheets with pore sizes of ~10 nm delivered a reversible capacity of 550 mA h $g^{-1}$ at 3.2 A $g^{-1}$ for SIBs, much higher than that of nonporous $Co_3O_4$ nanoplates (159 mA h $g^{-1}$),[32] due to the structural stability of 2D holey $Co_3O_4$ with small volume expansion (~6%) during the sodiation process. Moreover, thin SnS nanosheets with numerous tiny nanoclusters (~5 nm) and nanocavities (3–5 nm) constructed on flexible graphene foam exhibited a high reversible capacity (~1100 mA h $g^{-1}$ at 30 mA $g^{-1}$) and ultrafast sodium-ion diffusion kinetics generated by the intercalation pseudocapacitance (~420 mA h $g^{-1}$ at 30 A $g^{-1}$).[33] Notwithstanding the aforementioned progress to date, efficient synthesis of 2D holey and large-area cobalt sulfide nanosheets for SIBs has not yet been achieved.

Herein, we reported an efficient and scalable synthesis of 2D holey cobalt sulfide (h-$Co_4S_3$) nanosheets, derived from cobalt based metal–organic frameworks (CoMOFs) for long-life and high-rate SIBs. 2D h-$Co_4S_3$ nanosheets were synthesized *via* low-temperature hydrothermal sulfuration of CoMOFs, followed by annealing treatment. Notably, the resulting h-$Co_4S_3$ nanosheets feature in-plane nanopores (5–30 nm), ultra-thinness (<30 nm), crumpled morphology, and large lateral size (1–3 μm), all of which greatly reduced the diffusion lengths of the electrolyte and provided sufficient void space to buffer the volume expansion. As a result, the h-$Co_4S_3$ nanosheets for SIBs exhibit a high reversible capacity of 571 mA h $g^{-1}$ at 0.1 A $g^{-1}$, long cycling stability over 400 cycles in an ether-based electrolyte, and a high-rate capacity of 257 mA h $g^{-1}$ at 12 A $g^{-1}$, outperforming most reported cobalt sulfide-based anodes.

## Experimental section

### Material preparation

First, CoMOFs were synthesized in an aqueous system, as reported previously.[34,35] Typically, 40 mL $Co(NO_3)_2 \cdot 6H_2O$ (0.58 g) solution was added into 40 mL 2-methylimidazole (1.31 g), and the mixed solution was stirred at room temperature for 4 h. After centrifugation (6500 rpm for 5 min) and washing with water three times, the CoMOF product was dispersed in 140 mL water for subsequent sulfuration reaction. Solid CoMOFs could be harvested after washing and drying processes. Then, the as-prepared CoMOF dispersion was mixed with 40 mL of thioacetamide (TAA, 1.2 g) solution, and heated at 85 °C for 2 h under magnetic stirring. After that, the $CoS_x$ nanosheets were collected by centrifugation at 6500 rpm for 5 min, washed with water three times, and re-dispersed in 40 mL water for subsequent freeze drying. Finally, the 2D h-$Co_4S_3$ nanosheets were obtained by annealing treatment of $CoS_x$ nanosheets at 450 °C for 2 h in a nitrogen atmosphere.

### Materials characterization

Materials characterization was conducted by using Scanning electron microscopy (SEM, JEOL JSM-7800F), Transmission electron microscope (TEM) and high-resolution TEM (HRTEM, JEM-2100), Scanning transmission electron microscopy (STEM, FEI Tecnai G2 F20), X-ray diffraction (XRD, X'pert Pro), Raman spectroscopy (LabRam HR800 using a 633 nm laser), nitrogen sorption isotherm plots (Quadrasorb SI analyzer), thermogravimetric analysis (TGA, NETZSCH STA 449 F3) and X-ray photoelectron spectroscopy (XPS, Thermo ESCALAB 250Xi equipped with a monochromatic Al Kα source of 1486.5 eV).

### Electrochemical measurements

The tests of SIBs were carried out using CR2016 coin cells with sodium foil as the counter and reference electrodes, and 2D h-$Co_4S_3$ (or $CoS_x$) as the working electrode (12 mm in diameter), consisting of h-$Co_4S_3$ active material, carbon black, and polyvinylidene fluoride in a weight ratio of 7 : 2 : 1. The mass loading of the h-$Co_4S_3$ electrode is about ~0.7 mg $cm^{-2}$. SIB tests were conducted with 1.0 M $NaCF_3SO_3$ in diglyme (DGM) electrolyte or 1.0 M $NaClO_4$ in ethylene carbonate and dimethyl carbonate with 5% fluoroethylene carbonate (EC : DMC = 1 : 1, v : v with 5.0% FEC). Cyclic voltammetry (CV) studies were carried out on a CHI 760E electrochemical workstation at different scan rates within 0.5–3.0 V. Galvanostatic charge and discharge (GCD) profiles were recorded with a LAND CT2001A battery tester. Electrochemical impedance spectra were obtained using a CHI 660D workstation by applying an AC amplitude of 5 mV over the frequency range of 100 kHz to 0.01 Hz.

### Computational simulation

All calculations were performed with CASTEP code integrated into Materials Studio 6.0 package. A CoS (222) slab model containing 18Co and 18S atoms was constructed and the 222 facet was used as the reaction surface. Dimethyl ether (DE) and EC were considered as the adsorbates during the calculations. The binding energy ($E$) is defined as the energy difference between the slab model with an adsorbed molecule ($E_{total}$) and the summation of the adsorbed molecule ($E_1$) and slab system ($E_2$): $E = E_1 + E_2 - E_{total}$.

## Results and discussion

A schematic for synthesizing 2D h-$Co_4S_3$ nanosheets derived from CoMOFs is depicted in Fig. 1a. First, the violet CoMOFs with a leaf-like morphology were synthesized from $Co(NO_3)_2 \cdot 6H_2O$ and 2-methylimidazole in deionized water (Fig. S1a†).[35] Second, 2D large-area and amorphous $CoS_x$ ($x$ represents the unknown stoichiometric ratio of Co and S) nanosheets were prepared *via* sulfuration reaction of CoMOFs and thioacetamide (TAA) at 85 °C for 2 h. Finally, 2D h-$Co_4S_3$ nanosheets were obtained by annealing treatment of $CoS_x$ nanosheets at 450 °C for 2 h in nitrogen gas (Fig. S1b†).

SEM images of CoMOFs revealed the nature of leaf-like structure (Fig. 1b and S2†).[35] Interestingly, after TAA sulfuration, 2D crumpled large-area nanosheets were attained without any particle impurities (Fig. 1c and S3a†).

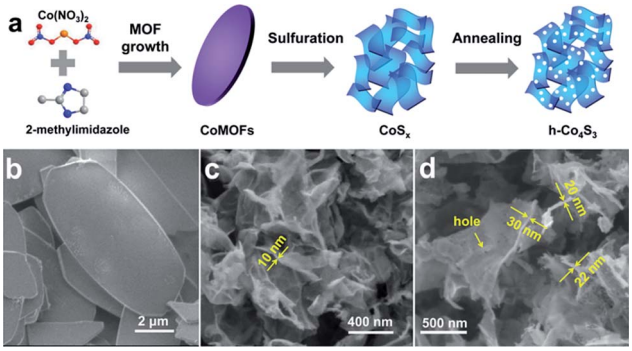


Fig. 1 (a) Schematic of the fabrication of 2D h-$Co_4S_3$ nanosheets, including the growth and sulfuration of CoMOFs, and annealing treatment of $CoS_x$ nanosheets. SEM images of (b) CoMOFs, (c) $CoS_x$ and (d) h-$Co_4S_3$ nanosheets.

Notably, the lateral size of $CoS_x$ nanosheets, with a thickness of 10–16 nm (Fig. S3b†), was in the micrometer scale (1–3 μm) (Fig. S3c†), larger than most reported cobalt based nanosheets (Table S1†), demonstrating the efficient synthesis of large-area cobalt sulfide nanosheets by the MOF-based strategy we developed here.[20,36–38] TEM images further reveal the 2D thinness and coarse wrinkled surface of $CoS_x$ nanosheets (Fig. 2a and S4†). It is worth noting that, from the control experiments, we found that (i) numerous small $CoS_x$ nanosheets first appeared on the surface of CoMOFs during initial sulfuration, *e.g.*, 10 min (Fig. S5†). With the extended sulfuration process, $CoS_x$ nanosheets of large lateral size grew continuously with the consumption of CoMOFs. (ii) CoMOFs, TAA and $H_2O$ played key roles in the formation of the $CoS_x$ nanosheets (Fig. S6 and S7†). The formation of $CoS_x$ nanosheets can be explained by the well-controlled kinetics between the dissolution of the CoMOFs and the growth of the $CoS_x$ (see details at the bottom of Fig. S6†).

After annealing treatment of $CoS_x$ nanosheets, the 2D structure was well preserved without any obvious decrease of lateral sizes (Fig. 1d, 2b–e and S8†). Interestingly, many in-plane holes, with diameters of several to tens of nanometers were formed (Fig. 2c and d), and the thickness of 2D holey nanosheets increased slightly to 20–30 nm (Fig. 1d). The HRTEM image showed the crystalline structure with a typical interlayer spacing of 0.29 nm, corresponding to the (100) lattice plane of $Co_4S_3$ (JCPDS no. 02-1458) (Fig. 2d). STEM with energy dispersive X-ray (EDX) elemental mapping analysis further demonstrated the existence of holes and uniform dispersions of Co and S in the survey region (Fig. 2e). The formation of holes in the h-$Co_4S_3$ nanosheets was mainly ascribed to the 2D plane contraction with enhanced thickness and crystalline structure accompanied by a certain amount of weight loss, as further confirmed by the product annealed at 350 °C (Fig. S9†).

The structural evolution from pristine CoMOFs to $CoS_x$ and h-$Co_4S_3$ nanosheets was elucidated using XRD patterns. As shown in Fig. 3a, the XRD pattern of CoMOFs validated the successful fabrication, in accordance with reported literatures.[34,35] After sulfuration reaction, $CoS_x$ nanosheets showed amorphous structures without any obvious diffraction peak. However, after annealing at 450 °C, the characteristic diffraction peaks, such as (100), (101), (102), and (110), assigned to $Co_4S_3$ appeared (JCPDS no. 02-1458). The Raman spectra of both $CoS_x$ and h-$Co_4S_3$ showed peaks at 473, 516, and 680 $cm^{-1}$, which were assigned to the $E_g$, $F_{2g}$, and $A_{1g}$ modes of cobalt sulfide (Fig. 3b),[19] respectively. The nitrogen adsorption–desorption isotherm of h-$Co_4S_3$ nanosheets further revealed the nature of mesopores (5–30 nm) and a higher specific surface area of 32 $m^2\ g^{-1}$ than that of $CoS_x$ (25 $m^2\ g^{-1}$) (Fig. 3c and d). The Co 2p XPS curves displayed two prominent Co–S peaks at 778.3 and 781.5 eV for the Co $2p_{3/2}$ signal, a minor peak of surface-adsorbed hydroxide at 786.4 eV originating from slight surface oxidation, and two peaks of Co $2p_{1/2}$ and a satellite signal at 791–810 eV.[19,37] The high-resolution S 2p corroborated the existence of Co–S bonding at 161.5 eV (S $2p_{3/2}$) and 162.6 eV (S $2p_{1/2}$) as well as oxidized surface sulfur at 166–172 eV.[37,39] These results demonstrate the successful fabrication of 2D holey h-$Co_4S_3$ nanosheets and introduction of mesopores into the plane of

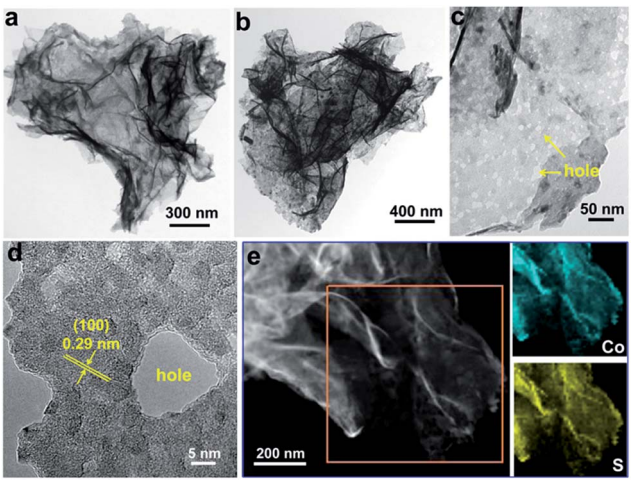


Fig. 2 (a) TEM images of $CoS_x$ nanosheets. (b and c) TEM and (d) HRTEM images of h-$Co_4S_3$ nanosheets. (e) STEM image of 2D h-$Co_4S_3$ nanosheets with the corresponding elemental mapping analysis of Co and S in the selected zone.

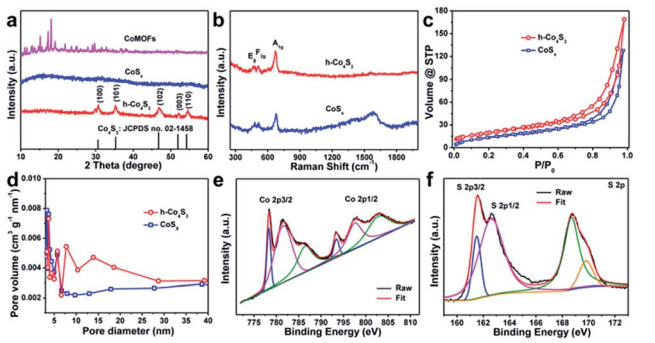


Fig. 3 Structural characterization of 2D h-$Co_4S_3$ nanosheets. (a) XRD patterns of CoMOFs, $CoS_x$ and h-$Co_4S_3$ nanosheets. (b) Raman spectra of $CoS_x$ and h-$Co_4S_3$ nanosheets. (c) Nitrogen adsorption–desorption isotherms and (d) pore size distribution of $CoS_x$ and h-$Co_4S_3$ nanosheets. (e) Co 2p and (f) S 2p XPS spectra of h-$Co_4S_3$ nanosheets.

ultrathin nanosheets, which are very helpful for offering a highly exposed surface for maximizing the material utilization, providing holey nanospaces for accommodating volume expansion, and facilitating rapid ion diffusion highways for enhancing the reaction kinetics of $Co_4S_3$ during cycling, thereby showing great potential for high performance SIBs.

To demonstrate this, we assembled a cell of SIB based on h-$Co_4S_3$ nanosheets as the working electrode, and sodium foil as the counter and reference electrodes in the ether-based electrolyte of 1.0 M $NaCF_3SO_3$ in DGM, and recorded the CV curves of the first three cycles (Fig. 4a), measured at 0.1 mV $s^{-1}$ between 0.5 and 3.0 V (*vs.* $Na^+$/Na). In the first discharge cycle, the cathodic peak at 1.2 V was commonly ascribed to an initial process of $Na^+$ insertion reaction of $Co_4S_3 + xNa^+ + xe^- \rightarrow Na_xCo_4S_3$, and the cathodic peak at 0.7 V was related to the conversion reaction of $Na_xCo_4S_3 + (6 - x)Na^+ + (6 - x)e^- \rightarrow 3Na_2S + 4Co$ and the formation of a solid electrolyte interphase.[22] Subsequently, the 2nd and 3rd cycle CV curves were almost overlapped at around 1.7 and 0.95 V, demonstrative of highly reversible electrochemical reactions. Remarkably, the h-$Co_4S_3$ anode delivered high reversible capacities of 571, 530 and 502 mA h $g^{-1}$ at the 1st, 3rd and 10th cycles, respectively, at 0.1 A $g^{-1}$ (Fig. 4b). Accordingly, the coulombic efficiency greatly increased from ~86% for the 1st cycle to ~101% for the 10th cycle. Furthermore, two distinct voltage plateaus at 1.0 V and 1.7 V appeared after the 1st cycle of the discharge profiles (Fig. 4b), well consistent with CVs (Fig. 4a). In sharp contrast, in the case of 1.0 M $NaClO_4$ in EC/DMC (1 : 1, v : v) with 5.0% FEC, the h-$Co_4S_3$ nanosheet anode showed fast capacity degradation from 1023 to 548.9 and 399 mA h $g^{-1}$, and lower coulombic efficiency from 58% to 90% and 82%, at the 1st, 3rd and 10th cycles (Fig. 4c). Moreover, h-$Co_4S_3$ exhibited a stable cycling performance in DGM based electrolyte, and after 150 cycles delivered a high capacity of 446 mA h $g^{-1}$ (Fig. 4d), much higher than that in EC/DEC based electrolyte (3.6 mA h $g^{-1}$). To elucidate the underlying mechanism to determine why sodium ion storage of cobalt sulfide in ether-based electrolyte is superior to that in carbonate-based electrolyte,[40–42] we further carried out density functional theory (DFT) calculations to understand their major disparity in sodium storage. From the model system containing 18Co and 18S atoms, it is calculated that the binding energy between DE and the CoS (222) slab model was 0.31 eV with a Co–O bond distance of 3.626 Å, while the binding energies between EC and CoS in two orientations of EC were 1.21 eV and 1.15 eV, corresponding to Co–O bond distances of 2.054 Å and 2.043 Å (Fig. 4e and f), respectively. These results suggested that there were strong interactions between EC and CoS, and the distorted crystal structure of cobalt sulfide was inclined to the lattice distortion in EC. Based on these findings, ether-based electrolyte would facilitate a stable electrode and stable formation of a solid electrolyte interphase (SEI) film for superior sodium storage.[41–43]

To further highlight the holey effect for fast ion diffusion across 2D nanosheets, the h-$Co_4S_3$ anode was tested at varying current densities from 0.05 A $g^{-1}$ to 12 A $g^{-1}$ (Fig. 5a). With increasing current density, remarkable reversible capacities were achieved from 558 mA h $g^{-1}$ (3rd cycle) at 0.05 A $g^{-1}$, 536 mA h $g^{-1}$ (7th cycle) at 0.1 A $g^{-1}$, 499 mA h $g^{-1}$ (12th cycle) at 0.5 A $g^{-1}$, 471 mA h $g^{-1}$ (17th cycle) at 1 A $g^{-1}$, 437 mA h $g^{-1}$ (22nd cycle) at 2 A $g^{-1}$, 391 mA h $g^{-1}$ (27th cycle) at 4 A $g^{-1}$, and 321 mA h $g^{-1}$ (32nd cycle) at 8 A $g^{-1}$ to 257 mA h $g^{-1}$ (37th cycle) at 12 A $g^{-1}$ (Fig. 5a and S10†), outperforming most reported cobalt sulfide hybrid anodes (Fig. 5b),[19,42,44–48] such as $Co_3S_4$ porous nanosheets embedded in graphene (307 mA h $g^{-1}$ at 2 A $g^{-1}$) and CoS hollow nanoparticles on carbon nanotubes

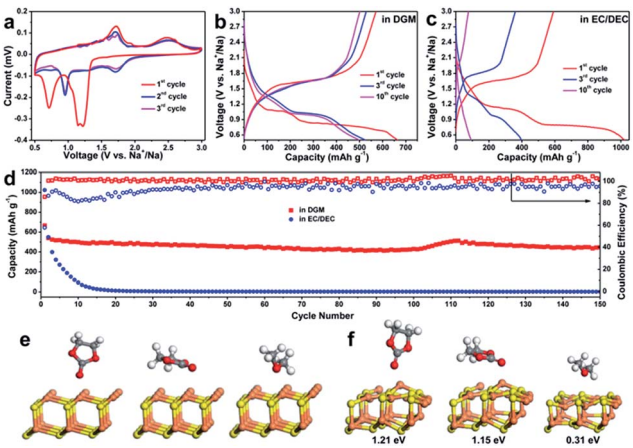


Fig. 4 Electrochemical characterization and computational simulation of 2D h-$Co_4S_3$ nanosheets for SIBs. (a) CV curves of the h-$Co_4S_3$ anode, measured at 0.1 mV $s^{-1}$ between 0.5 and 3.0 V in ether-based electrolyte (1.0 M $NaCF_3SO_3$ in DGM). (b and c) GCD profiles of the h-$Co_4S_3$ anode in (b) ether-based electrolyte and (c) carbonate-based electrolyte (1.0 M $NaClO_4$ in EC/DEC with 5% FEC). (d) Cycling stability of h-$Co_4S_3$ electrodes in DGM-based electrolyte and in carbonate based electrolyte, tested at 0.1 A $g^{-1}$. (e) The initial CoS (222) slab model and DE (right) or EC with two orientations (middle and left) before DFT calculations. (f) Binding energies between the CoS (222) slab model and DE (right) or EC with two orientations (middle and left) from DFT calculations.

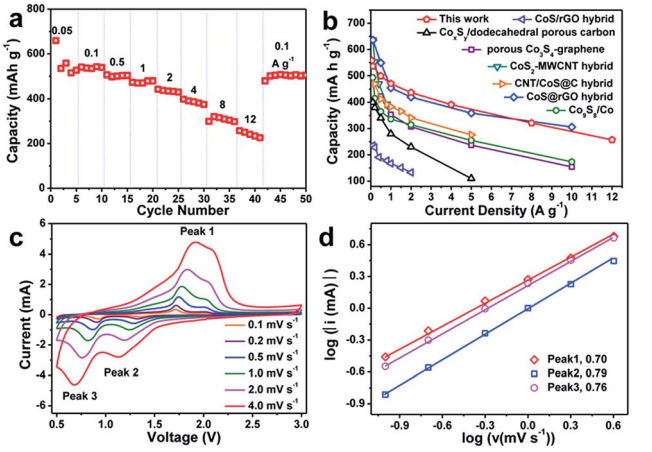


Fig. 5 Rate capability and pseudocapacitance characterization of 2D h-$Co_4S_3$ nanosheets for SIBs. (a) Rate capability of the h-$Co_4S_3$ anode at different current densities from 0.05 to 12 A $g^{-1}$. (b) Comparison of rate capabilities of h-$Co_4S_3$ nanosheets with other reported cobalt sulfide based electrodes. (c) CV curves tested at different scan rates and (d) the corresponding log *i versus* log *v* plots at each peak in (c).

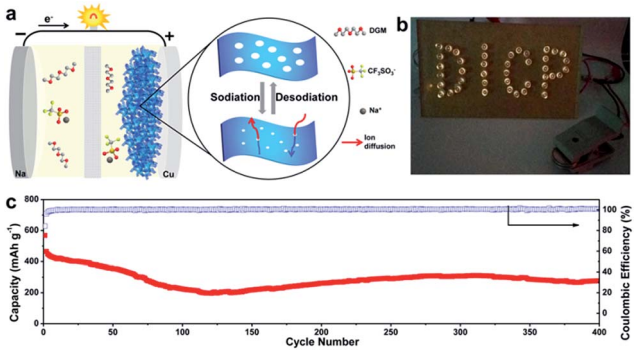


Fig. 6 (a) Schematic illustration of the rational design of the h-$Co_4S_3$ anode for SIBs. (b) Photograph of two tandem h-$Co_4S_3$ based SIB cells lighting up 42 LEDs. (c) Long-term cycling stability of the h-$Co_4S_3$ electrode, measured at 1 A $g^{-1}$.

(CNTs) (341 mA h $g^{-1}$ at 2 A $g^{-1}$, 276 mA h $g^{-1}$ at 5 A $g^{-1}$).[44,48] The electrochemical dynamics of the h-$Co_4S_3$ anode was further analyzed using CV curves acquired at different scan rates from 0.1 to 4 mV $s^{-1}$. The relation between peak current ($i$) and scan rate ($v$) could be expressed as $i = av^b$ or $\log(i) = b\log(v) + \log(a)$, where $a$ and $b$ are variable constants.[49] If the $b$ value ($0.5 < b < 1$) is close to 1, the electrochemical reaction is controlled by faradaic pseudocapacitance, otherwise the process is dominated by ionic diffusion when $b$ is close to 0.5. As shown in Fig. 5c, all the CV curves showed three prominent redox peaks, peak 1, peak 2 and peak 3, and the corresponding $b$ values were 0.70, 0.79, and 0.76, respectively, indicative of the huge pseudocapacitance contribution in h-$Co_4S_3$ anodes (Fig. 5d). Furthermore, two serially-connected cells of SIBs could easily power the letters of DICP consisting of 42 light-emitting diodes (LEDs) (Fig. 6a and b). Impressively, our h-$Co_4S_3$ electrodes still exhibited a high reversible capacity of 277 mA h $g^{-1}$ at a high current density of 1 A $g^{-1}$ after 400 cycles (Fig. 6c), suggestive of the tremendous potential in large scale applications.

The outstanding sodium-storage performance was attributed to the rational design of 2D h-$Co_4S_3$ nanosheets. First, the ultra-thinness of the h-$Co_4S_3$ nanosheets facilitated high utilization of the active material for high capacity SIBs. Second, the holey feature of the nanosheets greatly reduced the ion diffusion pathways across 2D nanosheets for fast sodiation and desodiation kinetics (Fig. 6a), as validated by the decreased charge-transport semicircle of h-$Co_4S_3$ at high frequency (Fig. S11†). Last, the in-plane mesoporous holey structure of the 2D nanosheets provided sufficient void nanospaces to accommodate volume expansion of h-$Co_4S_3$ during cycling (Fig. 6a, S12 and 13†), endowing the overall electrode with exceptional structural integrity for long durability.

## Conclusions

In summary, we demonstrated a versatile and efficient protocol for synthesizing CoMOF-derived 2D holey h-$Co_4S_3$ nanosheets for excellent sodium storage properties in an ether-based electrolyte. The ultrathin thickness (<30 nm) and numerous in-plane holes greatly facilitated fast sodiation/desodiation kinetics for achieving a high capacity of 257 mA h $g^{-1}$ at a high rate of 12 A $g^{-1}$, outperforming most cobalt sulfide hybrids. Meanwhile, the holey nanosheets could well accommodate the volume change of cobalt sulfide during charge/discharge cycles for long-term cycling stability with a retention of 80% after 400 cycles. Therefore, we believe that this MOF-based strategy will open new opportunities to rationally construct a large pool of advanced 2D holey nanosheets for various energy-related applications, *e.g.*, supercapacitors,[50] aluminum-ion batteries,[51] and lithium–air batteries.[52]

## Conflicts of interest

There are no conflicts to declare.

## Acknowledgements

This work was financially supported by the National Key R&D Program of China (Grants 2016YFB0100100 and 2016YFA0200200), National Natural Science Foundation of China (Grant 51572259), Natural Science Foundation of Liaoning Province (Grant 201602737), Recruitment Program of Global Expert (1000 Talent Plan), DICP (DICP ZZBS201708), Exploratory Research Program of Shaanxi Yanchang Petroleum (Group) CO., LTD & DICP, China Postdoctoral Science Foundation (Grants 2016M601349 and 2017T100188), DICP Outstanding Postdoctoral Foundation (2016YB06), and dedicated funds for methanol conversion from DICP.

## References

1 M. D. Slater, D. Kim, E. Lee and C. S. Johnson, *Adv. Funct. Mater.*, 2013, **23**, 947–958.
2 J.-Y. Hwang, S.-T. Myung and Y.-K. Sun, *Chem. Soc. Rev.*, 2017, **46**, 3529–3614.
3 J. Cui, S. Yao and J.-K. Kim, *Energy Storage Materials*, 2017, **7**, 64–114.
4 N. Yabuuchi, K. Kubota, M. Dahbi and S. Komaba, *Chem. Rev.*, 2014, **114**, 11636–11682.
5 Y. Li, Y. Lu, C. Zhao, Y.-S. Hu, M.-M. Titirici, H. Li, X. Huang and L. Chen, *Energy Storage Materials*, 2017, **7**, 130–151.
6 Y. Jiang, X. Zhou, D. Li, X. Cheng, F. Liu and Y. Yu, *Adv. Energy Mater.*, 2018, 1800068.
7 Y. Yin, F. Xiong, C. Pei, Y. Xu, Q. An, S. Tan, Z. Zhuang, J. Sheng, Q. Li and L. Mai, *Nano Energy*, 2017, **41**, 452–459.
8 Y. You, X.-L. Wu, Y.-X. Yin and Y.-G. Guo, *Energy Environ. Sci.*, 2014, **7**, 1643–1647.
9 J. Billaud, R. J. Clement, A. R. Armstrong, J. Canales-Vazquez, P. Rozier, C. P. Grey and P. G. Bruce, *J. Am. Chem. Soc.*, 2014, **136**, 17243–17248.
10 W. Luo, F. Li, J.-J. Gaumet, P. Magri, S. Diliberto, L. Zhou and L. Mai, *Adv. Energy Mater.*, 2018, 1703237.
11 J. Chen, S. Li, V. Kumar and P. S. Lee, *Adv. Energy Mater.*, 2017, 1700180.

12 K. Zhang, M. Park, L. Zhou, G.-H. Lee, J. Shin, Z. Hu, S.-L. Chou, J. Chen and Y.-M. Kang, *Angew. Chem., Int. Ed.*, 2016, **55**, 12822–12826.
13 C. Zhao, C. Yu, B. Qiu, S. Zhou, M. Zhang, H. Huang, B. Wang, J. Zhao, X. Sun and J. Qiu, *Adv. Mater.*, 2018, **30**, 1702486.
14 S. Liu, Y. Wang, Y. Dong, Z. Zhao, Z. Wang and J. Qiu, *ChemElectroChem*, 2016, **3**, 38–44.
15 C. Zhao, C. Yu, M. Zhang, H. Huang, S. Li, X. Han, Z. Liu, J. Yang, W. Xiao, J. Liang, X. Sun and J. Qiu, *Adv. Energy Mater.*, 2017, **7**, 1602880.
16 H. Hou, X. Qiu, W. Wei, Y. Zhang and X. Ji, *Adv. Energy Mater.*, 2017, **7**, 1602898.
17 Y. Xiao, S. H. Lee and Y.-K. Sun, *Adv. Energy Mater.*, 2017, **7**, 1601329.
18 Y. Zheng, T. Zhou, C. Zhang, J. Mao, H. Liu and Z. Guo, *Angew. Chem., Int. Ed.*, 2016, **55**, 3408–3413.
19 S. Peng, X. Han, L. Li, Z. Zhu, F. Cheng, M. Srinivansan, S. Adams and S. Ramakrishna, *Small*, 2016, **12**, 1359–1368.
20 H. Hu, B. Y. Guan and X. W. Lou, *Chem*, 2016, **1**, 102–113.
21 X.-Y. Yu, L. Yu and X. W. D. Lou, *Adv. Energy Mater.*, 2016, **6**, 1501333.
22 Q. Zhou, L. Liu, Z. Huang, L. Yi, X. Wang and G. Cao, *J. Mater. Chem. A*, 2016, **4**, 5505–5516.
23 X. Liu, K. Zhang, K. Lei, F. Li, Z. Tao and J. Chen, *Nano Res.*, 2016, **9**, 198–206.
24 Y. Xiao, J.-Y. Hwang, I. Belharouak and Y.-K. Sun, *Nano Energy*, 2017, **32**, 320–328.
25 W. Sun, X. Rui, D. Yang, Z. Sun, B. Li, W. Zhang, Y. Zong, S. Madhavi, S. Dou and Q. Yan, *ACS Nano*, 2015, **9**, 11371–11381.
26 Y. Dong, Z.-S. Wu, W. Ren, H.-M. Cheng and X. Bao, *Sci. Bull.*, 2017, **62**, 724–740.
27 C. Tan, X. Cao, X.-J. Wu, Q. He, J. Yang, X. Zhang, J. Chen, W. Zhao, S. Han, G.-H. Nam, M. Sindoro and H. Zhang, *Chem. Rev.*, 2017, **117**, 6225.
28 J. Mei, T. Liao, L. Kou and Z. Sun, *Adv. Mater.*, 2017, **29**, 1700176.
29 X. Wang, L. Lv, Z. Cheng, J. Gao, L. Dong, C. Hu and L. Qu, *Adv. Energy Mater.*, 2016, **6**, 1502100.
30 L. Peng, Z. Fang, Y. Zhu, C. Yan and G. Yu, *Adv. Energy Mater.*, 2018, **8**, 1702179.
31 H. Sun, L. Mei, J. Liang, Z. Zhao, C. Lee, H. Fei, M. Ding, J. Lau, M. Li, C. Wang, X. Xu, G. Hao, B. Papandrea, I. Shakir, B. Dunn, Y. Huang and X. Duan, *Science*, 2017, **356**, 599–604.
32 D. Chen, L. Peng, Y. Yuan, Y. Zhu, Z. Fang, C. Yan, G. Chen, R. Shahbazian-Yassar, J. Lu, K. Amine and G. Yu, *Nano Lett.*, 2017, **17**, 3907–3913.
33 D. Chao, C. Zhu, P. Yang, X. Xia, J. Liu, J. Wang, X. Fan, S. V. Savilov, J. Lin, H. J. Fan and Z. X. Shen, *Nat. Commun.*, 2016, **7**, 12122.
34 C. Guan, X. Liu, W. Ren, X. Li, C. Cheng and J. Wang, *Adv. Energy Mater.*, 2017, **7**, 1602391.
35 R. Chen, J. Yao, Q. Gu, S. Smeets, C. Baerlocher, H. Gu, D. Zhu, W. Morris, O. M. Yaghi and H. Wang, *Chem. Commun.*, 2013, **49**, 9500–9502.
36 W. Fu, C. Zhao, W. Han, Y. Liu, H. Zhao, Y. Ma and E. Xie, *J. Mater. Chem. A*, 2015, **3**, 10492–10497.
37 W. Chen, C. Xia and H. N. Alshareef, *ACS Nano*, 2014, **8**, 9531–9541.
38 L. Shen, J. Wang, G. Xu, H. Li, H. Dou and X. Zhang, *Adv. Energy Mater.*, 2015, **5**, 1400977.
39 Q. Guo, Y. Ma, T. Chen, Q. Xia, M. Yang, H. Xia and Y. Yu, *ACS Nano*, 2017, **11**, 12658–12667.
40 X. Wei, C. Tang, Q. An, M. Yan, X. Wang, P. Hu, X. Cai and L. Mai, *Nano Res.*, 2017, **10**, 3202–3211.
41 Y. Zhu, L. Suo, T. Gao, X. Fan, F. Han and C. Wang, *Electrochem. Commun.*, 2015, **54**, 18–22.
42 Z. Shadike, M.-H. Cao, F. Ding, L. Sang and Z.-W. Fu, *Chem. Commun.*, 2015, **51**, 10486–10489.
43 H. Che, S. Chen, Y. Xie, H. Wang, K. Amine, X.-Z. Liao and Z.-F. Ma, *Energy Environ. Sci.*, 2017, **10**, 1075–1101.
44 Y. Du, X. Zhu, X. Zhou, L. Hu, Z. Dai and J. Bao, *J. Mater. Chem. A*, 2015, **3**, 6787–6791.
45 Y. Zhao, Q. Pang, Y. Wei, L. Wei, Y. Ju, B. Zou, Y. Gao and G. Chen, *ChemSusChem*, 2017, **10**, 4778–4785.
46 Z. Zhang, Y. Gan, Y. Lai, X. Shi, W. Chen and J. Li, *RSC Adv.*, 2015, **5**, 103410–103413.
47 Q. Zhou, L. Liu, G. Guo, Z. Yan, J. Tan, Z. Huang, X. Chen and X. Wang, *RSC Adv.*, 2015, **5**, 71644–71651.
48 F. Han, C. Y. Jun Tan and Z. Gao, *J. Power Sources*, 2017, **339**, 41–50.
49 Y. Tang, Z. Zhao, X. Hao, Y. Wang, Y. Liu, Y. Hou, Q. Yang, X. Wang and J. Qiu, *J. Mater. Chem. A*, 2017, **5**, 13591–13600.
50 S. Peng, L. Li, H. Tian, R. Cai, W. Shi, C. Li, S. G. Mhaisalkar, M. Srinivasan, S. Ramakrishna and Q. Yan, *Adv. Funct. Mater.*, 2014, **24**, 2155–2162.
51 Y. Hu, D. Ye, B. Luo, H. Hu, X. Zhu, S. Wang, L. Li, S. Peng and L. Wang, *Adv. Mater.*, 2018, **30**, 1703824.
52 P. Sennu, M. Christy, V. Aravindan, Y.-G. Lee, K. S. Nahm and Y.-S. Lee, *Chem. Mater.*, 2015, **27**, 5726–5735.